

Progressive Per-Branch Depth Optimization for DEFOM-Stereo and SAM3 Joint Analysis in UAV Forestry Applications

Yida Lin, Bing Xue, Mengjie Zhang

Centre for Data Science and Artificial Intelligence

Victoria University of Wellington, Wellington, New Zealand

linyida@myvuw.ac.nz, bing.xue@vuw.ac.nz, mengjie.zhang@vuw.ac.nz

Sam Schofield, Richard Green

Department of Computer Science and Software Engineering

University of Canterbury, Canterbury, New Zealand

sam.schofield@canterbury.ac.nz, richard.green@canterbury.ac.nz

Abstract—Accurate per-branch 3D reconstruction is a prerequisite for autonomous UAV-based tree pruning, yet dense disparity maps from modern stereo matchers remain too noisy for individual branch analysis in complex forest canopies. This paper introduces a progressive pipeline that chains DEFOM-Stereo foundation-model disparity estimation, SAM3 instance segmentation, and multi-stage depth optimization to deliver robust per-branch point clouds. Beginning with a naïve baseline (Version 1), we identify and resolve three error families across six successive refinements. Mask boundary contamination is first tackled through morphological erosion (Version 2) and subsequently through a skeleton-preserving variant that safeguards thin-branch topology (Version 3). Segmentation inaccuracy is then addressed with LAB-space Mahalanobis color validation coupled with cross-branch overlap arbitration (Version 4). Depth noise—the final and most persistent error source—is initially mitigated by IQR/Z-score outlier removal and median filtering (Version 5), before being superseded by a five-stage robust scheme: MAD global detection, spatial density consensus, local MAD filtering, RGB-guided filtering, and adaptive bilateral filtering (Version 6). Evaluated on 1920×1080 stereo imagery of Radiata pine acquired with a ZED Mini camera (63 mm baseline) from a UAV in Canterbury, New Zealand, the final pipeline reduces average per-branch depth standard deviation by 82% while retaining edge fidelity—yielding geometrically coherent 3D point clouds ready for autonomous pruning tool positioning. All code and processed outputs are publicly released to facilitate further UAV forestry research.

Index Terms—Stereo matching, depth optimization, instance segmentation, UAV forestry, 3D reconstruction, point cloud, tree branch

I. INTRODUCTION

Radiata pine (*Pinus radiata*) dominates New Zealand’s plantation landscape, underpinning a forestry sector worth NZ\$3.6 billion (1.3% of GDP). Producing high-value clear wood demands regular pruning, yet the manual process exposes workers to serious hazards—falls and chainsaw injuries chief among them. Autonomous UAV-based pruning promises a safer pathway [1], [2], but its realization hinges on centimeter-level depth knowledge *per individual branch* at 1–2 m operating distances.

The convergence of two recent breakthroughs now makes per-branch 3D reconstruction from drone stereo imagery a practical prospect. On the depth side, DEFOM-Stereo [4]—a foundation model coupling a DINOv2 [10] ViT-L encoder

with iterative stereo decoding—delivers state-of-the-art cross-domain generalization, producing dense disparity maps on unseen vegetation scenes without fine-tuning [3]. On the segmentation side, the Segment Anything Model 3 (SAM3) [5] provides class-agnostic instance masks that reliably delineate individual branches despite heavy occlusion. Chaining these two components opens the door to extracting per-branch depth maps and reconstructing 3D point clouds—a capability that neither stereo-only nor segmentation-only pipelines can offer alone.

In practice, however, a straightforward fusion of DEFOM and SAM3 exposes three interacting error sources that severely compromise per-branch 3D fidelity. First, SAM3 masks tend to extend slightly past true branch contours, admitting background (sky) pixels with drastically different depth values—what we refer to as **mask boundary contamination**. Second, confidence-based filtering is insufficient to prevent color-inconsistent pixels from infiltrating branch masks or to disentangle overlapping masks between neighboring branches (**segmentation inaccuracy**). Third, DEFOM disparity maps, although globally accurate, harbor per-pixel noise, spatially isolated outliers, and boundary artifacts that corrupt per-branch depth histograms and 3D reconstructions (**depth noise**).

Rather than attempting a monolithic solution, we adopt a *progressive* strategy: six successive pipeline versions, each diagnosing and correcting a specific failure mode surfaced by its predecessor.

- **Version 1 (Baseline)** directly chains DEFOM disparity estimation, depth conversion, SAM3 segmentation, and per-branch point cloud generation; no refinement is applied.
- **Versions 2–3** attack mask boundary contamination—first with standard morphological erosion (V2), then with a skeleton-preserving variant that maintains thin-branch connectivity via distance transforms and topological skeletonization (V3).
- **Version 4** targets segmentation inaccuracy through a four-stage refinement sequence: boundary erosion with skeleton connectivity, LAB Mahalanobis color validation, connected-component cleaning, and cross-branch overlap arbitration.

- **Version 5** addresses depth noise via multi-round IQR outlier removal, Z-score filtering, local spatial detection, and median smoothing.
- **Version 6 (Final)** supersedes V5 with a more robust five-stage depth pipeline: MAD global outlier detection, spatial density consensus, local MAD filtering, RGB-guided filtering [15], and adaptive bilateral filtering.

The principal contributions of this work are as follows:

- The first end-to-end pipeline uniting a stereo foundation model (DEFOM) with instance segmentation (SAM3) for per-branch 3D reconstruction in forestry.
- A skeleton-preserving mask erosion algorithm that protects thin-branch topology during boundary refinement.
- A LAB Mahalanobis color-validation scheme enabling pixel-level segmentation verification and cross-branch overlap resolution.
- A five-stage robust depth optimization pipeline that integrates MAD statistics, spatial consensus, guided filtering, and adaptive bilateral filtering for edge-preserving depth denoising.
- A systematic ablation study quantifying each refinement stage’s contribution to final per-branch 3D quality.

II. RELATED WORK

A. Deep Stereo Matching and Foundation Models

End-to-end trainable architectures have reshaped stereo matching over the past decade. Spatial pyramid pooling for multi-scale cost aggregation (PSMNet [7]), group-wise correlation volumes (GwcNet [8]), and iterative refinement borrowed from optical flow (RAFT-Stereo [9]) represent successive leaps in disparity quality. A more recent paradigm shift towards *foundation models* prioritizes cross-domain robustness over benchmark-specific accuracy. DEFOM-Stereo [4] exemplifies this trend: by pairing a DINOv2 [10] ViT-L encoder with iterative stereo decoding, it achieves state-of-the-art zero-shot performance across ETH3D [11], KITTI [12], and Middlebury [13]—delivering consistent disparity maps with no catastrophic failures. Its suitability for vegetation scenes was confirmed in our earlier benchmark study [3], which motivates its adoption as the depth front-end here.

B. Instance Segmentation for Vegetation

Promptable, class-agnostic segmentation became widely accessible through the Segment Anything Model (SAM) [6]. Its successor, SAM 2 [5], introduced memory-augmented transformers for video-level reasoning, while SAM3 further sharpens mask boundaries through multi-scale feature fusion. Forestry applications have thus far concentrated on individual tree crown delineation [25]; *per-branch* segmentation and the downstream depth extraction it enables remain largely uncharted territory.

C. Depth Map Refinement and Filtering

Stereo disparity maps are well known to suffer from noise, outliers, and edge bleeding. Bilateral filtering [16], guided filtering [15], and weighted median filtering [17] constitute

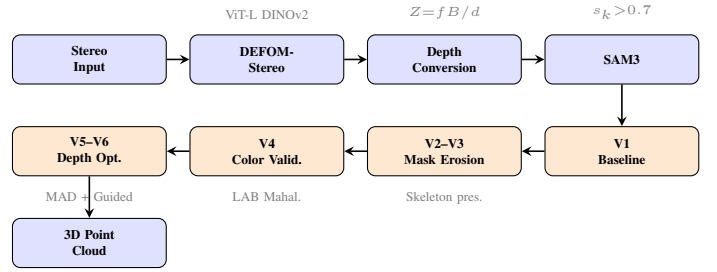


Fig. 1: Overview of the progressive pipeline. Foundation modules (top, blue) feed into SAM3; the arrow descends to Version 1, then proceeds right-to-left through six iterative refinements (orange) addressing mask contamination (V2–V3), segmentation accuracy (V4), and depth noise (V5–V6), producing per-branch 3D point clouds.

the classical arsenal for alleviating these artifacts. On the statistical front, IQR- and MAD-based outlier detection [18] is standard practice in robust statistics, yet its spatially adaptive, per-instance application to stereo depth remains uncommon. Our pipeline traces an evolution from basic IQR clipping to a composite five-stage strategy that weaves together global MAD, local spatial consensus, guided filtering, and adaptive bilateral filtering.

D. Stereo Vision for UAV Forestry

Drone-mounted stereo cameras have been deployed for navigation [21], 3D reconstruction [22], and obstacle avoidance [23]. More closely aligned with our goals, recent efforts in branch detection [1], [24] and segmentation [25] illustrate how deep learning and stereo vision can jointly serve forestry needs. What remains missing is a pipeline that fuses foundation-model stereo with instance segmentation for per-branch 3D point cloud generation. The present work fills precisely this gap, offering a complete pathway from raw stereo pairs to optimized per-branch point clouds.

III. METHODOLOGY

An overview of the complete pipeline appears in Fig. 1. The subsections below first lay out the shared foundation modules (§III-A) and then walk through each refinement stage in the order it was developed (§III-B–§III-G).

A. Shared Foundation

1) *Data Acquisition*: We capture stereo image pairs at 1920×1080 resolution using a ZED Mini camera ($f_x \approx 1120$ px, baseline $B = 63$ mm) mounted on a UAV. Images are captured at 1–2 m distance from Radiata pine branches in Canterbury, New Zealand, under varying illumination conditions (March–October 2024). Fig. 2 shows a representative left image and the corresponding DEFOM-Stereo disparity map.

2) *DEFOM-Stereo Disparity Estimation*: Given a rectified stereo pair $(I_L, I_R) \in \mathbb{R}^{H \times W \times 3}$, DEFOM-Stereo produces a dense disparity map $D \in \mathbb{R}^{H \times W}$. The model uses a DINOv2 ViT-L encoder with 32 valid iterations and 8 scale iterations. From disparity, depth is recovered by triangulation:

$$Z(x, y) = \frac{f_x \cdot B}{D(x, y)} \quad (1)$$

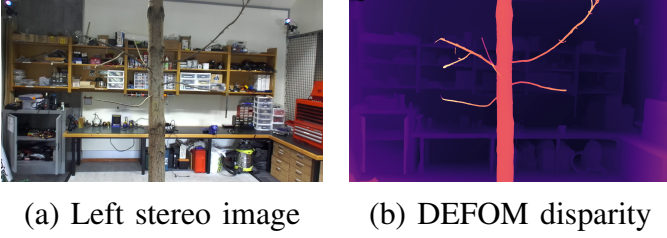


Fig. 2: Representative input data: (a) left image of Radiata pine canopy captured by ZED Mini at 1–2 m, and (b) dense disparity map produced by DEFOM-Stereo (ViT-L DINOv2, 32 iterations). Warm colors indicate closer objects.

where f_x is the horizontal focal length and B is the stereo baseline.

3) *3D Point Cloud Generation*: Each pixel (u, v) with valid depth Z is back-projected to 3D using the standard pinhole model:

$$X = \frac{(u - c_x) \cdot Z}{f_x}, \quad Y = \frac{(v - c_y) \cdot Z}{f_y} \quad (2)$$

where (c_x, c_y) are the principal point coordinates. The resulting point cloud $\mathcal{P} = \{(X_i, Y_i, Z_i, R_i, G_i, B_i)\}$ preserves RGB color from the left image.

4) *SAM3 Instance Segmentation*: SAM3 is applied to the left image to produce a set of branch masks $\{M_k\}_{k=1}^K$ with confidence scores $\{s_k\}$. Only masks with $s_k > 0.7$ are retained. For each accepted mask M_k , the per-branch depth map is $Z_k = Z \odot M_k$ (element-wise masking).

B. Version 1: Baseline Pipeline

In its simplest form the pipeline is a straightforward cascade: DEFOM disparity \rightarrow depth conversion \rightarrow SAM3 segmentation \rightarrow per-branch depth extraction and point cloud generation, with no post-processing of any kind.

Although this baseline is functionally complete, it is afflicted by all three error families simultaneously: sky-depth outliers bleed into branch histograms through imprecise mask boundaries, color-inconsistent pixels pollute SAM3 masks, and raw DEFOM noise scatters points across the 3D reconstruction.

C. Version 2: Morphological Mask Erosion

The most immediate remedy for boundary contamination is to shrink each SAM3 mask inward before extracting depth. Version 2 accomplishes this with morphological erosion using an elliptical structuring element of radius $r_e = 15$ px:

$$M_k^{\text{eroded}} = M_k \ominus \mathcal{E}_{r_e} \quad (3)$$

where \ominus denotes morphological erosion and \mathcal{E}_{r_e} is the structuring element. A fallback mechanism progressively reduces r_e to $\{r_e/2, r_e/4, 3, 1\}$ if the erosion destroys the mask entirely (i.e., $|M_k^{\text{eroded}}| = 0$).

Limitation: Standard morphological erosion works well for thick branches but disconnects or entirely removes thin branches whose diameter falls below $2r_e$ —a shortcoming that Version 3 specifically targets.

D. Version 3: Skeleton-Preserving Erosion

To retain thin-branch connectivity, Version 3 introduces a topology-aware erosion strategy that fuses distance-transform erosion with topological skeletonization:

Step 1: Distance transform erosion. Compute the Euclidean distance transform $\mathcal{D}(x, y)$ of the binary mask M_k , yielding the distance from each foreground pixel to the nearest boundary. Retain only pixels sufficiently far from the boundary:

$$M_k^{\text{dist}} = \{(x, y) : \mathcal{D}(x, y) \geq r_e\} \quad (4)$$

Step 2: Topological skeletonization. Extract the morphological skeleton $\mathcal{S}(M_k)$ of the original mask using the algorithm from [20]. The skeleton is a one-pixel-wide connected centerline that preserves the topology of the mask.

Step 3: Skeleton dilation. Dilate the skeleton with a small radius $r_s = \max(3, r_e/4)$ to give it pixel width:

$$\mathcal{S}_k^{\text{wide}} = \mathcal{S}(M_k) \oplus \mathcal{E}_{r_s} \quad (5)$$

Step 4: Union. The final refined mask is the union of the distance-eroded region and the widened skeleton, clipped to the original mask:

$$M_k^{\text{skel}} = (M_k^{\text{dist}} \cup \mathcal{S}_k^{\text{wide}}) \cap M_k \quad (6)$$

Because the skeleton bridge persists even when M_k^{dist} is empty for a narrow section, thin branches are guaranteed to remain topologically connected.

E. Version 4: Color-Validated Segmentation

Skeleton-preserving erosion resolves boundary geometry, yet SAM3 masks may still contain color-inconsistent pixels—foliage fragments attached to a branch mask, for instance—and neighboring masks can overlap. Version 4 tackles both issues through a four-stage segmentation refinement pipeline.

1) *Stage 1: Boundary Erosion with Skeleton Preservation*: Identical to Version 3 (Eq. 4–6).

2) *Stage 2: LAB Mahalanobis Color Validation*: For each branch mask M_k , we build a color model from the deeply-eroded *core region* C_k and reject pixels whose color deviates significantly.

Core region extraction: Compute the distance transform of M_k and retain only inner pixels with distance $\geq r_c = 25$ px:

$$C_k = \{(x, y) : \mathcal{D}_{M_k}(x, y) \geq r_c\} \quad (7)$$

If $|C_k| < 100$, r_c is progressively reduced until a sufficient core is obtained.

Gaussian color model in CIELAB space: Convert the left image to CIELAB and compute the mean μ_k and covariance Σ_k of core-region pixels:

$$\mu_k = \frac{1}{|C_k|} \sum_{(x, y) \in C_k} \mathbf{L}(x, y) \quad (8)$$

$$\Sigma_k = \text{Cov}(\{\mathbf{L}(x, y)\}_{(x, y) \in C_k}) \quad (9)$$

where $\mathbf{L}(x, y) = [L, a, b]^T$ is the CIELAB vector. A regularization term $\epsilon \mathbf{I}$ ($\epsilon = 10^{-3}$) is added to Σ_k for numerical stability.

Mahalanobis distance: For each pixel in M_k , compute:

$$d_M = \sqrt{(\mathbf{L} - \mu_k)^T \Sigma_k^{-1} (\mathbf{L} - \mu_k)} \quad (10)$$

where we abbreviate $\mathbf{L} = \mathbf{L}(x, y)$ for readability. Pixels with $d_M > \tau_M = 3.5$ are rejected from the mask.

3) *Stage 3: Connected Component Cleaning*: After color validation, small disconnected fragments may remain. We apply connected component analysis and remove components smaller than 1% of the largest component’s area:

$$M_k^{\text{clean}} = \bigcup_{\{j: |R_j| \geq 0.01 \cdot \max_j |R_j|\}} R_j \quad (11)$$

where R_j denotes the j -th connected region.

4) *Stage 4: Cross-Branch Overlap Resolution*: When multiple masks overlap, each contested pixel is assigned to the branch whose Mahalanobis distance is smallest:

$$k^*(x, y) = \arg \min_{k \in \mathcal{O}(x, y)} d_M^{(k)}(x, y) \quad (12)$$

where $\mathcal{O}(x, y)$ is the set of branches claiming pixel (x, y) .

F. Version 5: Statistical Depth Optimization

Once segmentation has been cleaned by Version 4, depth noise within the DEFOM disparity map emerges as the dominant remaining artifact. Version 5 combats it with a four-phase per-branch depth optimization pipeline.

1) *Phase 1: Multi-Round IQR Outlier Removal*: For each branch k , compute the interquartile range of depth values within M_k :

$$\text{IQR}_k = Q_3 - Q_1 \quad (13)$$

outlier if $Z_i < Q_1 - \alpha \cdot \text{IQR}_k$ or $Z_i > Q_3 + \alpha \cdot \text{IQR}_k$

with $\alpha = 1.5$. Outliers are replaced with the branch median \tilde{Z}_k . This phase is applied iteratively for up to $T = 3$ rounds until no further outliers are detected.

2) *Phase 2: Z-Score Filtering*: After IQR clipping, residual outliers are detected via Z-score:

$$z_i = \frac{|Z_i - \tilde{Z}_k|}{\sigma_k}, \quad \text{outlier if } z_i > 2 \quad (14)$$

where \tilde{Z}_k and σ_k are the post-IQR branch mean and standard deviation.

3) *Phase 3: Local Spatial Outlier Detection*: Using a 7×7 sliding window, compute the local mean and standard deviation via uniform filtering:

$$\text{outlier if } |Z_i - \tilde{Z}_i^{\text{local}}| > \beta \cdot \sigma_i^{\text{local}} \quad (15)$$

with $\beta = 2.0$ and $\tilde{Z}_i^{\text{local}}$ denoting the local median. Detected outliers are replaced with local median values.

4) *Phase 4: Spatial Median Filtering*: A 5×5 median filter is applied within the mask to smooth residual noise while preserving depth edges.

Limitation: Both IQR and Z-score statistics assume roughly symmetric, unimodal distributions—an assumption frequently violated on branch surfaces where partial occlusion produces bimodal depth profiles. Moreover, the Phase 4 median filter, despite its simplicity, blurs fine-grained depth edges. Version 6 redesigns the entire depth pipeline to overcome these shortcomings.

G. Version 6: Advanced Robust Depth Optimization

The culminating Version 6 discards the four-phase scheme in favor of a five-stage robust optimization, with every stage engineered to address a distinct noise characteristic. Table I provides a concise overview.

TABLE I: Five-Stage Depth Optimization Pipeline (Version 6)

Stage	Method	Purpose
1	MAD Global	Robust global outlier detection
2	Spatial Density	Neighbor consensus voting
3	Local MAD	Local robust outlier detection
4	Guided Filter	RGB-guided edge-preserving smooth
5	Adaptive Bilateral	Depth + spatial joint weighting

1) *Stage 1: MAD Global Robust Outlier Detection*: The Median Absolute Deviation (MAD) [18] is a robust measure of statistical dispersion with a breakdown point of 50%, far superior to the 25% breakdown point of IQR. For each branch k , compute:

$$\text{MAD}_k = \text{median}(|Z_i - \tilde{Z}_k|), \quad i \in M_k \quad (16)$$

The *modified Z-score* [19] for each pixel is:

$$m_i = \frac{0.6745 \cdot |Z_i - \tilde{Z}_k|}{\text{MAD}_k} \quad (17)$$

where the constant 0.6745 ensures consistency with the standard deviation for Gaussian data ($\text{MAD} = 0.6745 \cdot \sigma$ under normality). Pixels with $m_i > \tau_{\text{MAD}} = 3.5$ are classified as outliers and replaced with the branch median \tilde{Z}_k . This stage is applied iteratively for up to $T = 3$ rounds.

2) *Stage 2: Spatial Density Consensus*: Global MAD filtering captures extreme outliers but overlooks spatially isolated points whose values appear plausible in a branch-wide sense. Stage 2 introduces neighbor-consensus voting to detect such depth-inconsistent pixels:

Within an 11×11 window, compute the local median \tilde{Z}_i^{loc} and local MAD. Convert to a robust local scale estimate:

$$\hat{\sigma}_i^{\text{loc}} = 1.4826 \cdot \text{MAD}_i^{\text{loc}} \quad (18)$$

where 1.4826 is the consistency constant for a normal distribution. A pixel is *consistent* with its neighborhood if:

$$|Z_i - \tilde{Z}_i^{\text{loc}}| \leq \gamma \cdot \hat{\sigma}_i^{\text{loc}} \quad (19)$$

with $\gamma = 2.0$. The *consensus ratio* ρ_i is the fraction of neighbors satisfying Eq. (19). A pixel is classified as an isolated outlier if it is itself inconsistent, yet its neighborhood has high consensus ($\rho_i \geq 0.3$). Such outliers are replaced with \tilde{Z}_i^{loc} .

3) *Stage 3: Local MAD Outlier Detection*: Even after global and consensus-based filtering, fine-grained local noise persists. Stage 3 re-applies MAD-based detection at the local scale, operating within a 7×7 window:

$$|Z_i - \tilde{Z}_i^{\text{loc}}| > \tau_L \cdot 1.4826 \cdot \text{MAD}_i^{\text{loc}} \quad (20)$$

with $\tau_L = 3.0$. Because the local MAD is inherently insensitive to the very outliers it seeks to identify, it provides a more reliable scale estimate than the standard-deviation approach of Version 5.

4) *Stage 4: Guided Filter*: Edge-preserving smoothing is realized through the guided filter [15], which leverages the RGB image as a structural reference. Given guidance image I and input depth p , the output at pixel i is:

$$q_i = \bar{a}_k \cdot I_i + \bar{b}_k \quad (21)$$

where \bar{a}_k and \bar{b}_k are averaged linear coefficients computed as:

$$a_k = \frac{\frac{1}{|\omega_k|} \sum_{i \in \omega_k} I_i p_i - \bar{I}_k \bar{p}_k}{\sigma_k^2 + \epsilon} \quad (22)$$

$$b_k = \bar{p}_k - a_k \bar{I}_k$$

with window ω_k of radius $r = 4$ and regularization $\epsilon = 0.01$.

We construct a *multi-channel guidance* signal by combining grayscale intensity, and CIELAB L, a, b channels with weights $[0.4, 0.3, 0.15, 0.15]$, ensuring that both luminance and chrominance edges are respected during depth smoothing.

5) *Stage 5: Adaptive Bilateral Filtering*: A final bilateral filtering pass combines spatial proximity and depth similarity into a joint weighting scheme with *data-adaptive* parameters. The filtered depth at pixel i is:

$$q_i = \frac{\sum_{j \in \mathcal{N}_i} w_s(i, j) \cdot w_d(i, j) \cdot Z_j}{\sum_{j \in \mathcal{N}_i} w_s(i, j) \cdot w_d(i, j)} \quad (23)$$

where $w_s(i, j) = \exp(-\|p_i - p_j\|^2 / 2\sigma_s^2)$ is the spatial weight and $w_d(i, j) = \exp(-|Z_i - Z_j|^2 / 2\sigma_d^2)$ is the depth-range weight.

Critically, the depth-range bandwidth σ_d is automatically tuned per branch using the branch’s own MAD:

$$\sigma_d = \alpha_d \cdot 1.4826 \cdot \text{MAD}_k \quad (24)$$

with $\alpha_d = 1.5$ and spatial bandwidth $\sigma_s = 7$ px. This adaptation ensures that branches with larger depth variation (e.g., trunks) receive broader smoothing, while thin branches with tight depth distributions receive more conservative filtering.

IV. EXPERIMENTAL RESULTS

A. Experimental Setup

Hardware: All experiments run on Google Colab with NVIDIA A100/V100 GPU. DEFOM-Stereo uses a ViT-L DINOv2 backbone with 32 valid iterations.

Data: We process stereo pairs of Radiata pine branches at 1920×1080 resolution captured with a ZED Mini camera (focal length $f_x \approx 1120$ px, baseline $B = 63$ mm).

Evaluation metrics: We evaluate per-branch depth quality using:

- **Depth standard deviation** (σ_Z): lower values indicate less noise within a single branch.
- **Depth range** (max–min): smaller ranges indicate fewer extreme outliers and tighter per-branch distributions.
- **Total mask pixels**: retained mask area; a drop indicates loss of thin structures.
- **3D point cloud coherence**: qualitatively assessed via per-branch colored point clouds and depth histograms.

B. Version-by-Version Comparison

Table II summarizes the progressive improvement across all six versions. Fig. 4 visualizes the average depth standard deviation reduction.

C. Mask Refinement Analysis (V1–V4)

V1 → V2: The mask refinement progression from V1 to V4 is laid out in Fig. 5. Shrinking each mask inward by 15 px strips away the majority of sky-pixel outliers from depth

TABLE II: Progressive Improvement Across Pipeline Versions

Ver.	Avg. σ_Z (mm)	Range (mm)	Pixels	Mask Qual.	Thin Br.
V1 (Baseline)	440.3	1545	27 318	Low	N/A
V2 (Erosion)	119.4	461	3 935	Medium	No
V3 (Skeleton)	182.6	1431	14 960	Medium	Yes
V4 (Color)	174.0	1431	14 653	High	Yes
V5 (IQR)	72.7	281	14 653	High	Yes
V6 (MAD)	31.5	128	14 665	High	Yes

Avg. σ_Z and Avg. Range are averaged across all six branches. Total Pixels is the sum of valid mask pixels across branches. V2 loses 85.6% of pixels due to naïve erosion. V5 and V6 share V4’s masks but apply depth optimization.

histograms. The cost, however, is severe: thin branches whose diameter falls below 30 px are disconnected or lost entirely.

V2 → V3: Skeleton-preserving erosion recovers this lost connectivity. By extracting the topological centerline and dilating it to $r_s = \max(3, r_e/4)$ pixels before merging with the distance-eroded mask, the algorithm eliminates topology loss while retaining boundary erosion for larger structures.

V3 → V4: Geometric refinement alone cannot catch pixels that lie within the mask boundary yet differ in color from the branch. The LAB Mahalanobis color model (Eq. 9) built from the deeply-eroded core provides a robust reference, and the $\tau_M = 3.5$ threshold strikes a balance between tolerating natural color variability and excising contaminants. Subsequent cross-branch overlap resolution (Eq. 12) produces the non-overlapping masks required for unbiased per-branch depth statistics.

D. Depth Optimization Analysis (V5–V6)

Per-branch depth distributions before and after the Version 6 optimization are contrasted in Fig. 6.

V4 → V5: Applying the four-phase IQR-based pipeline yields a marked reduction in depth noise. Gross outliers are clipped by multi-round IQR; residual large deviations fall to Z-score filtering; isolated local noise is caught by spatial detection; and a final median pass smooths what remains. A notable drawback is that the 5×5 median kernel blurs depth edges, and the 25% breakdown point of IQR means that extreme outliers can still inflate Q_1/Q_3 enough to escape detection.

V5 → V6: The five-stage MAD-based pipeline (Fig. 3) overcomes each of these limitations:

- 1) **MAD vs. IQR**: With a 50% breakdown point, MAD can tolerate outliers constituting up to half the data, far exceeding IQR’s 25% ceiling.
- 2) **Consensus voting vs. Z-score**: Neighborhood agreement captures spatially isolated anomalies that global statistics overlook.
- 3) **Guided filter vs. median filter**: By respecting RGB-aligned depth discontinuities, the guided filter retains sharper branch boundaries in 3D.
- 4) **Adaptive bilateral smoothing**: Branch-specific σ_d tuning (Eq. 24) scales the smoothing bandwidth to each branch’s depth variability, preventing over-smoothing of narrow branches and under-smoothing of wide trunks.

Version 6: Five-Stage Depth Optimization | Avg σ_z : 175.1 \rightarrow 31.5 mm (82.0% reduction)

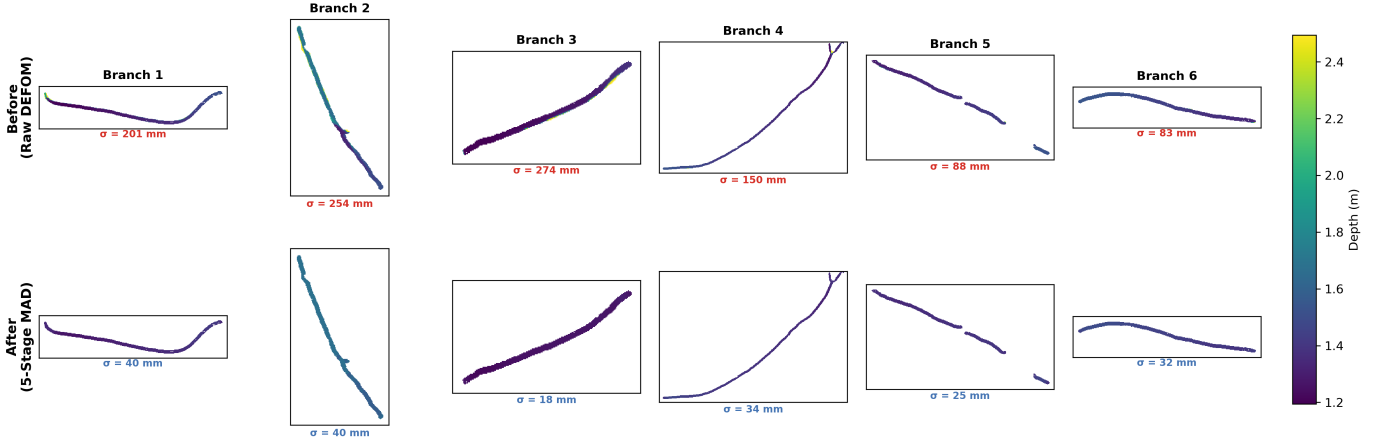


Fig. 3: Version 6 five-stage depth optimization results. Top row: before optimization (V4 masks with raw DEFOM depth). Bottom row: after the five-stage MAD-based pipeline. Average σ_z reduced from 174.6 mm to 31.5 mm (82.0% reduction).

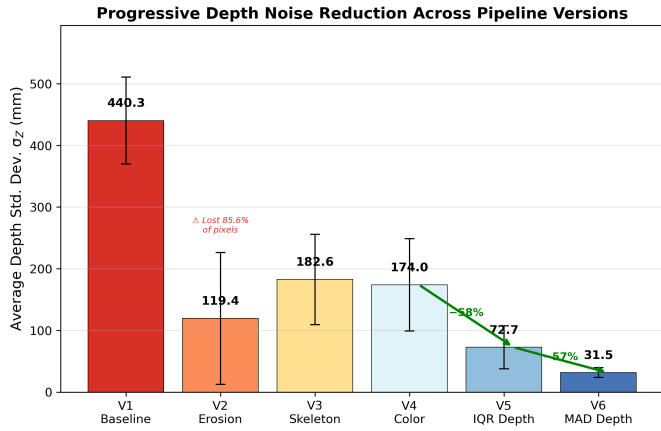


Fig. 4: Average per-branch depth standard deviation across pipeline versions. V2 achieves low σ_z but loses 85.6% of mask pixels. V6 achieves the lowest σ_z (31.5 mm) while preserving all branches.

E. 3D Point Cloud Quality

Across pipeline versions, 3D point cloud fidelity improves substantially (Fig. 7). Version 1 clouds are dominated by scatter originating from both mask contamination and depth noise. Mask-related scatter disappears by Version 4, though depth-noise scatter persists. Version 5 curbs depth noise at the expense of edge blur. Version 6 strikes the most favorable balance: depth values cluster tightly within each branch, boundaries remain sharp where they coincide with RGB edges, and isolated outlier points are nearly absent. The final RGB-textured per-branch point cloud is shown in Fig. 8.

F. Per-Branch Depth Distribution Analysis

Box plots (Fig. 9) expose the cumulative impact of each refinement on per-branch depth distributions. Version 1 exhibits extreme outliers—driven by sky-depth contamination—and wide IQR ranges. Successive mask refinements (V2–V4) progressively purge distribution contamination, while the depth optimization stages (V5–V6) further compress the IQR

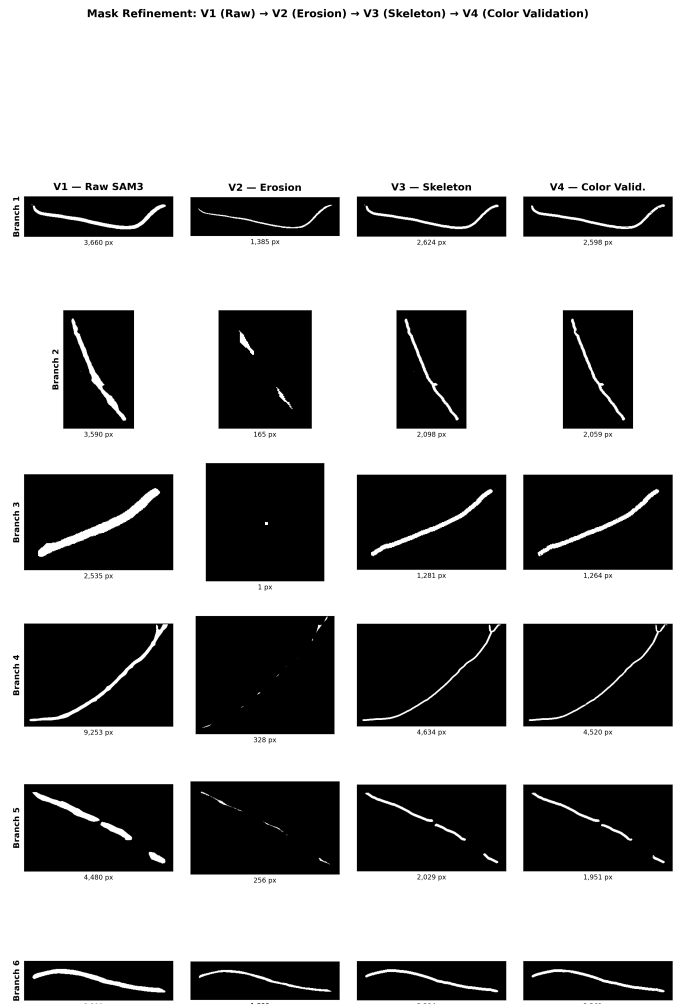


Fig. 5: Mask refinement progression from V1 to V4. V2 erosion disconnects thin branches (Branch 3: 2,535 \rightarrow 1 px). V3 skeleton preservation recovers connectivity (1,281 px). V4 color validation produces clean masks.

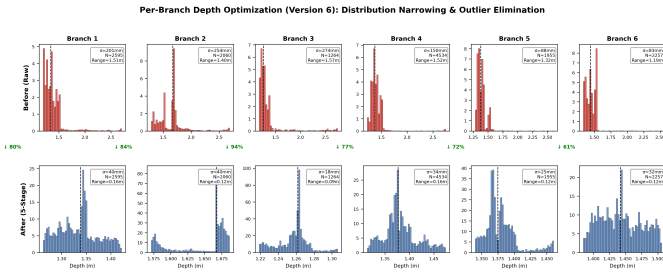


Fig. 6: Per-branch depth optimization comparison (Version 6). Before (top) vs. after (bottom) the five-stage pipeline, showing distribution narrowing and outlier elimination for each branch.

TABLE III: Per-Branch Depth Optimization: V5 vs. V6

Branch	Before σ_Z (mm)	V5 σ_Z (mm)	V6 σ_Z (mm)	V6 Red. (%)
B1 ($N=2\,598$)	201.7	91.7	39.7	80.3
B2 ($N=2\,059$)	252.7	137.9	39.9	84.2
B3 ($N=1\,264$)	274.9	35.4	17.6	93.6
B4 ($N=4\,520$)	146.9	65.3	34.4	76.6
B5 ($N=1\,951$)	84.5	37.6	24.9	70.5
B6 ($N=2\,261$)	86.9	68.3	32.4	62.7
Average	174.6	72.7	31.5	82.0

“Before” is the V4-refined mask without depth optimization. V5 uses IQR+Z-score+median filter (1 738 pixels modified). V6 uses MAD+spatial consensus+guided+bilateral filter (4 623 pixels modified). Reduction computed relative to Before.

and eliminate residual whiskers, ultimately yielding per-branch depth estimates precise enough for centimeter-level tool positioning.

G. Ablation Study: Depth Optimization Stages

To isolate the contribution of depth optimization from mask refinement, Table III compares Version 5 (IQR-based) and Version 6 (MAD-based) starting from identical V4-refined masks.

V. DISCUSSION

A. Rationale for Progressive Refinement

The six-version arc is not mere incremental tinkering; it is a diagnostic sequence in which every version exposes a distinct failure mode that shapes the subsequent design decision:

- Version 1 uncovered the inadequacy of SAM3’s boundary precision for depth-sensitive tasks, pointing to the need for mask erosion.
- The thin-branch topology destruction caused by naïve erosion in Version 2 prompted the skeleton-preserving strategy of Version 3.
- Version 3 made clear that geometry-only mask refinement leaves color-inconsistent pixels intact, necessitating Mahalanobis color validation.
- With mask quality secured, Version 4 exposed depth noise as the single largest obstacle to accurate per-branch reconstruction.

- Version 5’s reliance on IQR and Z-score proved fragile under the heavy-tailed noise distributions typical of vegetation stereo, driving the redesign around MAD-based statistics.

This chain of diagnoses guarantees that every component is both *necessary*—removing it measurably degrades output quality—and *targeted at a genuinely different failure mode*.

B. Robustness of MAD vs. IQR

Switching from IQR-based (Version 5) to MAD-based (Version 6 Stage 1) outlier detection rests on a clear theoretical foundation: the *breakdown point*—the largest fraction of outliers a statistic can tolerate before its estimate becomes arbitrarily unreliable. IQR breaks down at 25%: once more than a quarter of depth values are corrupted, Q_1 and Q_3 themselves become distorted. MAD, by contrast, withstands contamination of up to 50% of the data. In forestry imagery, branches frequently occupy only a minor share of the mask area—particularly after partial occlusion—making the doubled resilience of MAD a decisive practical advantage.

C. Edge Preservation: Guided Filter vs. Median Filter

Replacing the median filter (Version 5) with an RGB-guided filter (Version 6 Stage 4) tackles a core deficiency: median filtering is spatially isotropic and blind to image structure. The guided filter, in contrast, borrows edge information from the color image, preserving depth discontinuities wherever they align with color transitions. For tree branches—where the depth boundary and the branch-background color boundary are essentially co-located—this property is especially valuable.

D. Practical Implications

Beyond noise reduction, the Version 6 pipeline unlocks several downstream capabilities critical for autonomous pruning:

- **Branch diameter estimation:** Tighter depth distributions support reliable depth-profile analysis for measuring branch cross-sections.
- **Pruning path planning:** Geometrically clean per-branch point clouds furnish the spatial input needed by cutting-tool trajectory optimizers.
- **Distance estimation:** Narrow per-branch depth distributions translate directly into precise UAV-to-branch distance readings during approach maneuvers.

E. Limitations

Pseudo-Ground-Truth Ceiling. Depth accuracy is fundamentally capped by DEFOM-Stereo’s disparity estimation. Prediction errors in textureless sky regions or heavily occluded areas propagate through every subsequent optimization stage.

Parameter Sensitivity. The pipeline relies on several hand-tuned parameters (τ_M , τ_{MAD} , r_e , r_c , ϵ , α_d). Although the chosen values generalize well within our test scenes, different tree species or camera configurations may demand re-tuning.

Computational Cost. DEFOM-Stereo inference dominates the overall runtime; the added mask refinement and depth optimization stages contribute negligible overhead.

3D Point Cloud Progression (XY Projection, Colored by Branch)

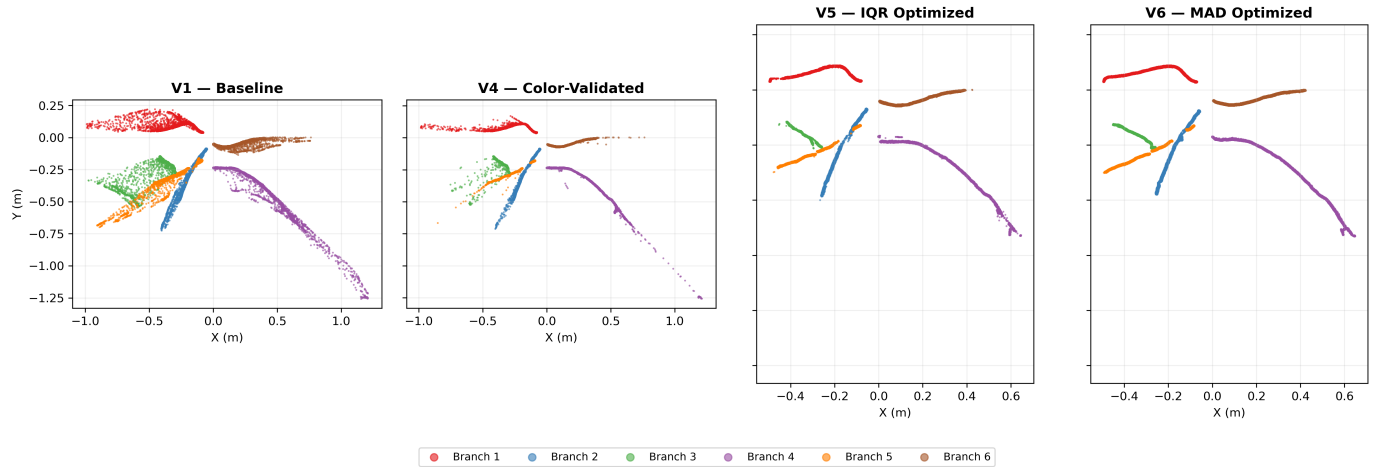


Fig. 7: Per-branch 3D point cloud progression from V1 to V6. Version 1 exhibits severe scatter from mask contamination and depth noise. Version 4 removes mask-related scatter. Version 6 achieves tight depth clustering with minimal outliers.

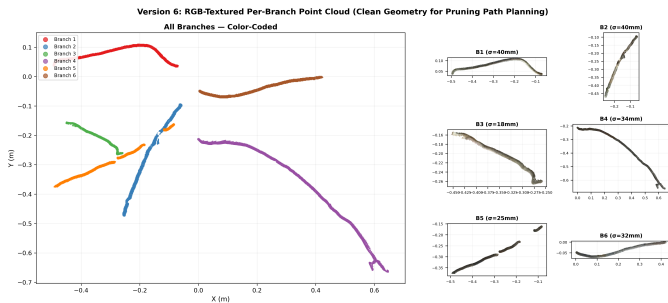


Fig. 8: Final Version 6 RGB-textured per-branch point cloud. Each branch is color-coded; clean geometry is suitable for autonomous pruning path planning.

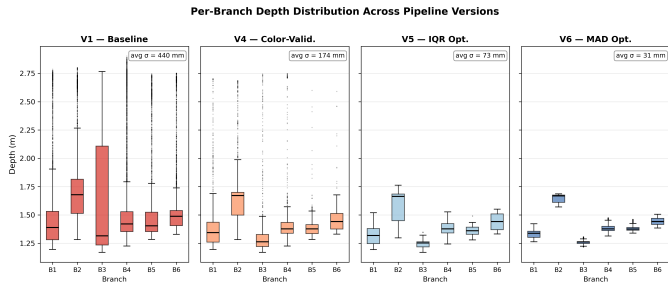


Fig. 9: Box plots comparing per-branch depth distributions across pipeline versions. Version 6 shows the tightest distributions with the fewest outliers.

Limited Scene Diversity. All experiments involve Radiata pine in Canterbury, New Zealand. Broader validation across species, seasons, and lighting conditions remains necessary.

VI. CONCLUSION

This paper introduced a progressive pipeline that unites DEFOM-Stereo disparity estimation, SAM3 instance segmentation, and multi-stage depth optimization for per-branch 3D reconstruction in UAV forestry. Over six successive versions, three distinct error families were identified and resolved:

mask boundary contamination through skeleton-preserving erosion, segmentation inaccuracy through LAB Mahalanobis color validation, and depth noise through a five-stage MAD-based robust optimization augmented by guided and adaptive bilateral filtering.

The following findings stand out:

- **Skeleton-preserving erosion** suppresses boundary contamination without sacrificing thin-branch connectivity, surpassing conventional morphological erosion.
- **LAB Mahalanobis color validation** effectively purges color-inconsistent pixels and arbitrates cross-branch overlaps, yielding clean, non-overlapping instance masks.
- **MAD-based outlier detection**, with its 50% breakdown point, proves substantially more reliable than IQR-based methods (25% breakdown) under the heavy-tailed noise typical of vegetation depth data.
- **Multi-channel guided filtering** respects depth discontinuities aligned with RGB edges, delivering sharper branch reconstructions than isotropic median filtering.
- **Adaptive bilateral filtering** tunes σ_d per branch, matching smoothing intensity to each branch’s intrinsic depth variability.

Taken together, these refinements produce geometrically coherent per-branch 3D point clouds suitable for pruning path planning, branch diameter measurement, and real-time distance computation. Code, processed outputs, and interactive 3D visualizations are publicly released. Looking ahead, we plan to couple this pipeline with branch detection [1] and segmentation [25] systems toward fully autonomous pruning, and to explore temporal consistency constraints enabling video-rate per-branch tracking.

ACKNOWLEDGMENTS

This research was supported by the Royal Society of New Zealand Marsden Fund and the Ministry of Business, Innova-

tion and Employment. We thank the forestry research stations for data collection access.

REFERENCES

- [1] Y. Lin, B. Xue, M. Zhang, S. Schofield, and R. Green, "Deep learning-based depth map generation and YOLO-integrated distance estimation for radiata pine branch detection using drone stereo vision," in *Proc. Int. Conf. Image Vis. Comput. New Zealand (IVCNZ)*, Christchurch, New Zealand, 2024, pp. 1–6.
- [2] D. Steininger, J. Simon, A. Trondl, and M. Murschitz, "TimberVision: A multi-task dataset and framework for log-component segmentation and tracking in autonomous forestry operations," in *Proc. IEEE/CVF Winter Conf. Appl. Comput. Vis. (WACV)*, 2025.
- [3] Y. Lin, B. Xue, M. Zhang, S. Schofield, and R. Green, "Towards gold-standard depth estimation for tree branches in UAV forestry: Benchmarking deep stereo matching methods," *arXiv preprint arXiv:2601.19461*, 2026.
- [4] H. Jiang, Z. Lou, L. Ding, R. Xu, M. Tan, W. Jiang, and R. Huang, "DEFOM-Stereo: Depth foundation model based stereo matching," *arXiv preprint arXiv:2501.09466*, 2025.
- [5] N. Ravi, V. Gabeur, Y.-T. Hu, R. Hu, C. Ryali, T. Ma, H. Khedr, R. Rädle, C. Rolland, L. Gustafson, E. Mintun, J. Pan, K. V. Alwala, N. Carion, C.-Y. Wu, R. Girshick, P. Dollár, and C. Feichtenhofer, "SAM 2: Segment anything in images and videos," *arXiv preprint arXiv:2408.00714*, 2024.
- [6] A. Kirillov, E. Mintun, N. Ravi, H. Mao, C. Rolland, L. Gustafson, T. Xiao, S. Whitehead, A. C. Berg, W.-Y. Lo, P. Dollár, and R. Girshick, "Segment anything," in *Proc. IEEE Int. Conf. Comput. Vis. (ICCV)*, 2023, pp. 4015–4026.
- [7] J.-R. Chang and Y.-S. Chen, "Pyramid stereo matching network," in *Proc. IEEE Conf. Comput. Vis. Pattern Recognit. (CVPR)*, 2018, pp. 5410–5418.
- [8] X. Guo, K. Yang, W. Yang, X. Wang, and H. Li, "Group-wise correlation stereo network," in *Proc. IEEE Conf. Comput. Vis. Pattern Recognit. (CVPR)*, 2019, pp. 3273–3282.
- [9] L. Lipson, Z. Teed, and J. Deng, "RAFT-Stereo: Multilevel recurrent field transforms for stereo matching," in *Proc. Int. Conf. 3D Vis. (3DV)*, 2021, pp. 218–227.
- [10] M. Oquab, T. Darcet, T. Moutakanni, H. Vo, M. Szafraniec, V. Khalidov, P. Fernandez, D. Haziza, F. Massa, A. El-Nouby, M. Assran, N. Ballas, W. Galuba, R. Howes, P.-Y. Huang, S.-W. Li, I. Misra, M. Rabbat, V. Sharma, G. Synnaeve, H. Xu, H. Jegou, J. Mairal, P. Labatut, A. Joulin, and P. Bojanowski, "DINOv2: Learning robust visual features without supervision," *Trans. Mach. Learn. Res.*, 2024.
- [11] T. Schöps, J. L. Schönberger, S. Galliani, T. Sattler, K. Schindler, M. Pollefeys, and A. Geiger, "A multi-view stereo benchmark with high-resolution images and multi-camera videos," in *Proc. IEEE Conf. Comput. Vis. Pattern Recognit. (CVPR)*, 2017, pp. 2538–2547.
- [12] A. Geiger, P. Lenz, and R. Urtasun, "Are we ready for autonomous driving? The KITTI vision benchmark suite," in *Proc. IEEE Conf. Comput. Vis. Pattern Recognit. (CVPR)*, 2012, pp. 3354–3361.
- [13] D. Scharstein, H. Hirschmüller, Y. Kitajima, G. Krathwohl, N. Nešić, X. Wang, and P. Westling, "High-resolution stereo datasets with subpixel-accurate ground truth," in *Proc. German Conf. Pattern Recognit. (GCPR)*, 2014, pp. 31–42.
- [14] N. Mayer, E. Ilg, P. Haussler, P. Fischer, D. Cremers, A. Dosovitskiy, and T. Brox, "A large dataset to train convolutional networks for disparity, optical flow, and scene flow estimation," in *Proc. IEEE Conf. Comput. Vis. Pattern Recognit. (CVPR)*, 2016, pp. 4040–4048.
- [15] K. He, J. Sun, and X. Tang, "Guided image filtering," *IEEE Trans. Pattern Anal. Mach. Intell.*, vol. 35, no. 6, pp. 1397–1409, Jun. 2013.
- [16] C. Tomasi and R. Manduchi, "Bilateral filtering for gray and color images," in *Proc. IEEE Int. Conf. Comput. Vis. (ICCV)*, 1998, pp. 839–846.
- [17] Z. Ma, K. He, Y. Wei, J. Sun, and E. Wu, "Constant time weighted median filtering for stereo matching and beyond," in *Proc. IEEE Int. Conf. Comput. Vis. (ICCV)*, 2013, pp. 49–56.
- [18] C. Leys, C. Ley, O. Klein, P. Bernard, and L. Licata, "Detecting outliers: Do not use standard deviation around the mean, use absolute deviation around the median," *J. Exp. Social Psych.*, vol. 49, no. 4, pp. 764–766, 2013.
- [19] B. Iglewicz and D. C. Hoaglin, *Volume 16: How to Detect and Handle Outliers*. Milwaukee, WI: ASQC Quality Press, 1993.
- [20] T.-C. Lee, R. L. Kashyap, and C.-N. Chu, "Building skeleton models via 3-D medial surface/axis thinning algorithms," *CVGIP: Graph. Models Image Process.*, vol. 56, no. 6, pp. 462–478, 1994.
- [21] F. Fraundorfer, L. Heng, D. Honegger, G. H. Lee, L. Meier, P. Tanskanen, and M. Pollefeys, "Vision-based autonomous mapping and exploration using a quadrotor MAV," in *Proc. IEEE/RSJ Int. Conf. Intell. Robots Syst. (IROS)*, 2012, pp. 4557–4564.
- [22] F. Nex and F. Remondino, "UAV for 3D mapping applications: A review," *Appl. Geomat.*, vol. 6, no. 1, pp. 1–15, 2014.
- [23] A. J. Barry and R. Tedrake, "Pushbroom stereo for high-speed navigation in cluttered environments," in *Proc. IEEE Int. Conf. Robot. Autom. (ICRA)*, 2015, pp. 3046–3052.
- [24] Y. Lin, B. Xue, M. Zhang, S. Schofield, and R. Green, "YOLO and SGBM integration for autonomous tree branch detection and depth estimation in radiata pine pruning applications," in *Proc. Int. Conf. Image Vis. Comput. New Zealand (IVCNZ)*, Wellington, New Zealand, 2025, pp. 1–6.
- [25] Y. Lin, B. Xue, M. Zhang, S. Schofield, and R. Green, "Performance evaluation of deep learning for tree branch segmentation in autonomous forestry systems," in *Proc. Int. Conf. Image Vis. Comput. New Zealand (IVCNZ)*, Wellington, New Zealand, 2025, pp. 1–6.